Journal of Alloys and Compounds 959 (2023) 170244

Contents lists available at ScienceDirect

Journal of Alloys and Compounds

journal homepage: www.elsevier.com/locate/jalcom

Sol-gel synthesis control of iron-cobalt alloy/ferrite core/shell nanoparticles supported by a carbon medium with semi-hard magnetic features

Alberto Castellano-Soria [a,b,*], Jesús López-Sánchez [c,d], Aida Serrano [e], Giulio Gorni [f,g], María Varela [b,h], Ignacio Sardinero [d], Noemí Carmona [a,b], Antonio Hernando [a,b], Pilar Marín [a,b], Elena Navarro [a,b]

[a] Instituto de Magnetismo Aplicado (IMA-UCM-ADIF), 28230 Madrid, Spain
[b] Departamento de Física de Materiales, Facultad de Físicas, Universidad Complutense de Madrid (UCM), 28040 Madrid, Spain
[c] SpLine, Spanish CRG BM25 Beamline, ESRF-The European Synchrotron, 38000 Grenoble, France
[d] Instituto de Ciencia de Materiales de Madrid (ICMM-CSIC), 28049 Madrid, Spain
[e] Instituto de Cerámica y Vidrio (CSIC), 28049 Madrid, Spain
[f] CELLS-ALBA Synchrotron Light Facility, E-08290 Cerdanyola del Vallès, Spain
[g] Instituto de Óptica (IO-CSIC), 28006, Madrid, Spain
[h] Instituto Pluridisciplinar, Universidad Complutense de Madrid (UCM), 28040 Madrid, Spain

ARTICLE INFO

Article history:
Received 23 March 2023
Received in revised form 17 April 2023
Accepted 21 April 2023
Available online 25 April 2023

Keywords:
Sol-gel
Nanoparticles
Core/shell nanostructures
Fe-Co alloy
Spring-exchange. Semi-hard magnetic properties

ABSTRACT

We explore a simple and optimized approach for obtaining magnetic nanoparticle-carbon composites by a novel one-pot sol-gel method. In them, various metal cations ratios of Fe^{3+} and Co^{2+} are evaluated. The ratio of Fe:Co is a critical parameter that governs the presence of different crystalline phases with tailored magnetic properties. Interestingly, the smallest introduction of Co into the synthesis (19Fe:1Co) provides an abrupt emergence of the body-centered cubic (bcc) Fe-Co alloy, instead of the orthorhombic *Pnma* structure characteristic of the Fe_3C intermetallic compound (1Fe:0Co). Advanced structural and electronic characterizations reveal the formation of Fe-Co/Co-ferrite core/shell nanoparticle structures embedded in a carbon matrix. The sphere-like nanoparticles range from 10 to 45 nm and the shells show a spinel structure with a thickness of 2–3 nm. In addition, X-ray absorption spectroscopy unveils that the oxidation state of Fe and Co cations is close to zero, demonstrating their predominant metallic character. The magnetic properties can be modulated by a precise control of the alloy composition varying the Co content, displaying saturation magnetization values close to ~137 emu/g. The nanoparticles are mainly single magnetic domain with a considerable coercive field (~450 Oe), higher than those reported in the literature for Fe-Co nanoparticles. This semi-hard character is due to a notable spring exchange effect emerged by passivating the surface of Fe-Co-bcc cores with a thin Co-ferrite-like shell.

1. Introduction

In the current fervent study of nanostructured magnetic materials, metal-carbon-based ones have provided a wide field of research [1–3]. More specifically, standing out from magnetic oxides, carbide-based magnetic nanoparticles (M-NPs) such as the iron carbide (cementite, Fe_3C) have attracted interest by combining two highly functional properties induced by the carbon presence, i.e., a superior chemical stability compared to that displayed by metallic Fe, and good magnetic properties when it is alloyed with other metals. Subsequently, in the paradigm of magnetic optimization properties, the body-centered cubic (bcc) Fe-Co alloy is a ferromagnetic material (FM) known to reach the highest saturation magnetization (M_s) value (~240 emu/g for permendur, $Fe_{50}Co_{50}$), displaying a large permeability and an elevated Curie temperature (~1100 K) [4,5]. The alloy shows a soft magnetic character due to its low magneto-crystalline anisotropy values, close to ~20 kJ/m^3 [6–8]. Moreover, the excellent and potential magnetic properties of the Fe-Co alloys with NP morphology have ensued a great interest in nano-application fields like biomedicine as highly sensitive tracers for magnetic-particle-imaging (MPI) [9], magnetic fluid hyperthermia

* Corresponding author at: Instituto de Magnetismo Aplicado (IMA-UCM-ADIF), 28230 Madrid, Spain.
E-mail address: albcas04@ucm.es (A. Castellano-Soria).

https://doi.org/10.1016/j.jallcom.2023.170244

[10], and photothermal drug delivery [11]; as supporting media for enhanced catalysis, electrocatalysis, and magneto-assisted catalysis [12–15]; and as efficient microwave absorption [16,17], magnetorheological fluids [18], and spintronics [19].

Hence, many efforts have been devoted to the synthesis and control of magnetic properties of this alloy covering a wide variety of methods. From solid state methods, Fe-Co alloys are obtained by methane chemical vapor deposition (M-CVD) [20], pulsed laser deposition (PLD) [21,22], sputtering [8,23], and mechanical alloying [24]. In turn, chemical methods such as metal-powder assisted-reduction [18] and sol-gel-based synthesis [25] have also been employed. These approaches combine both high control of the alloys, simply by adding or changing the starting materials salts, and scalability and reproducibility of the nanomaterials obtained [26]. Among these, the polyol route performed in an alkaline medium and some variants, are the most widespread scalable synthesis procedures that provide good control in NP morphologies and size-distributions [15,27–32]. The polyol synthesis (basic media) commonly offers higher sizes for the obtained NPs (80–300 nm). By contrast, the sol-gel method is performed in acid pH and considerably reduces the particle sizes up to ~10–70 nm. It is usually based on macromolecules or biopolymers [33–35], polyol with post-annealing method [7,26], or wet impregnation and co-precipitation techniques [36]. In this sense, small NPs could be advantageous in the framework of the hardening-engineering of magnetic materials. Other variants, like the microemulsion-method [6], also shows narrow particle size distributions (PSDs) and small sizes < 10 nm. These are comparable with the crystalline quality of CVD methods, but results in NPs with a softer magnetic character than those above described.

The tuning and optimization of the magnetic properties of Fe-Co alloyed systems has also provided a wide field of fundamental research too. Recent *ab-initio* density-functional theory (DFT) studies have theoretically explored other alternatives as intermetallic compounds like $Fe_{3-x}Co_xC$ substitutional phases of the orthorhombic *Pnma* structure of the Fe_3C with crystalline anisotropies around hundreds of kJ/m^3 [37]. Although the presence of Co as substitutional solute increases the instability of cementite [38,39], some experimental evidence demonstrates that $Fe_{3-x}Co_xC$ NPs can be obtained by chemical-synthesis methods with substitutional values of $x < 0.3$ [40] or even higher [41]. In any case, a broad investigation about its structural characterization, compositional control, and reproducibility, is needed to understand the relevance of this complex system. Furthermore, other *ab-initio* studies have predicted a stable body-centered tetragonal (bct) phase for Fe-Co with C impurities, showing a magneto-crystalline anisotropy comparable with Fe-Pt alloys (~750 kJ/m^3). Therefore, C-based Fe-Co alloys could be perfect candidates for improving the properties of rare-earth-free permanent magnet applications [42,43].

Furthermore, experimental confirmations of the stabilized Fe-Co bcc phase are found in: i) a thin film of 100 nm via V and N addition by a dc-magnetron co-sputtering, displaying a value of 1.24 MJ/m^3 [44], ii) AuCu/FeCo core/shell NPs by inducing a tetragonal distortion that changes the coercive field (H_c) from 54 to 627 Oe by a reordering of the cores when are annealed at 380 ºC [45]. These examples are promising results but the desired scalability for industrial transference has not been reached yet. However, other approaches based on reduction of Fe_2CoO_4 have provided successful results increasing the hardness of such Fe-Co-bcc alloy through the spring-exchange effect at the interface between the core and the shell in FM/FM ($FeCo/Fe_2CoO_4$) NPs, but with elevated contents of oxide phase that degrades their M_s values [46,47]. Therefore, a full-understanding of the magnetic properties of Fe-Co alloyed systems, the optimization of its magnetic hardness, and the reproducibility and scalability of product materials by low-cost synthesis methods are currently a challenging field of study.

In this work, we address some of those issues by exploring a synthesis approach to obtain Fe-Co NPs based on a sol-gel macromolecule-surfactant method for fine-tuning their magnetic properties. Different metal cations ratios of Fe^{3+} and Co^{2+} are introduced in the synthesis ranging from 1:0, 19:1, 5:1, 2:1 and 1:2 (Fe:Co). An advanced structural, electronic, and magnetic characterization of the composites is carried out. The magnetic properties correspond with a semi-hard magnetic carbon composite, displaying an elevated M_s around 137 emu/g and enhanced H_c values around 450 Oe. This semi-hard character is due to the spring exchange effect between the soft FM core and the semi-hard FM shell. The presence of the Co-ferrite detected (~8%) is much lower than in recent reports (~ 20, 40 wt%) [47,48], indicating a highly effective shell capping for the hardening of the Fe-Co-bcc cores. A review of the state-of-the-art of the coercivity of this type of Fe-Co nanoparticles shows the remarkable magnetic properties of the ones presented in this work. This fact could offer potentially multifunctional properties of interest for future applications.

2. Experimental techniques

2.1. Synthesis of the Fe-Co/Co-ferrite core/shell nanoparticles by sol-gel

The NPs embedded in carbon matrix have been prepared through a novel sol-gel synthesis based on the use of large linear chains of organic molecules as surfactants with elevated and similar boiling points: oleic acid (OA, 360 ºC) and oleylamine (ON, 364 ºC). The hydrated nitrates $Fe(NO_3)_3{\cdot}9\ H_2O$ (Alfa Aesar +98%) and $Co(NO_3)_2{\cdot}6\ H_2O$ (Alfa Aesar +98%) were used as salt precursors. Firstly, they were completely dissolved in 50 mL of absolute ethanol (PanReac +99%) with a specific ratio Fe^{3+}:Co^2 and keeping a fixed sum amount of 12 mmol between Fe and Co ions. Then, the dissolution was left for 15 min at 40 ºC under a vigorous magnetic stirring. Subsequently, HNO_3 was added as catalyst until pH~ 1–2. Secondly, 5 mmol of ON (ACROS Organics 80–90%) were added dropwise and, after 15 min, the same quantity of OA (Sigma-Aldrich 90%). The resulting solution was maintained for 24 h under stirring. Then, the temperature was raised up to 75 ºC for 36 h to dry the sol-gel. Finally, the xerogel obtained was introduced in a horizontal tube furnace under a N_2 atmosphere. The densification process was performed at a rate of 5 ºC/min up to 700 ºC and it was kept at this temperature for 1 h. Finally, the obtained material was milled using an agate mortar.

2.2. Morphological, structural, electronic, and magnetic characterization

Crystal structure was examined by synchrotron X-ray diffraction (SXRD) measurements carried out at the beamline BM25 of the European Synchrotron Radiation Facility (ESRF) in Grenoble (France). The incident X-ray radiation used was 15 keV (λ = 0.8266 Å). The powders were introduced in a spinning quartz capillary (0.5 mm diameter) and the acquisition was performed in the 2θ range 8–57.5°, with 0.0075º steps. A 2D photon-counting X-ray *MAXIPIX* detector was employed, and the data were processed with the *BINoculars* software [49,50]. The crystal structure, lattice parameters, compositional percentage of phases and volume-weighted average crystallite size of the samples were inferred from Rietveld refinements, which were performed using the Profex interface of BGMN Rietveld software [51].

Morphological features, crystalline structure, particle size distribution (PSD), and compositional analysis of the nanostructures encased in the carbon matrix were analyzed by high resolution scanning transmission electron microscopy (STEM) combined with electron energy-loss spectroscopy (EELS), using a JEOL JEM ARM200cf with a cold field emission source, working with a CEOS

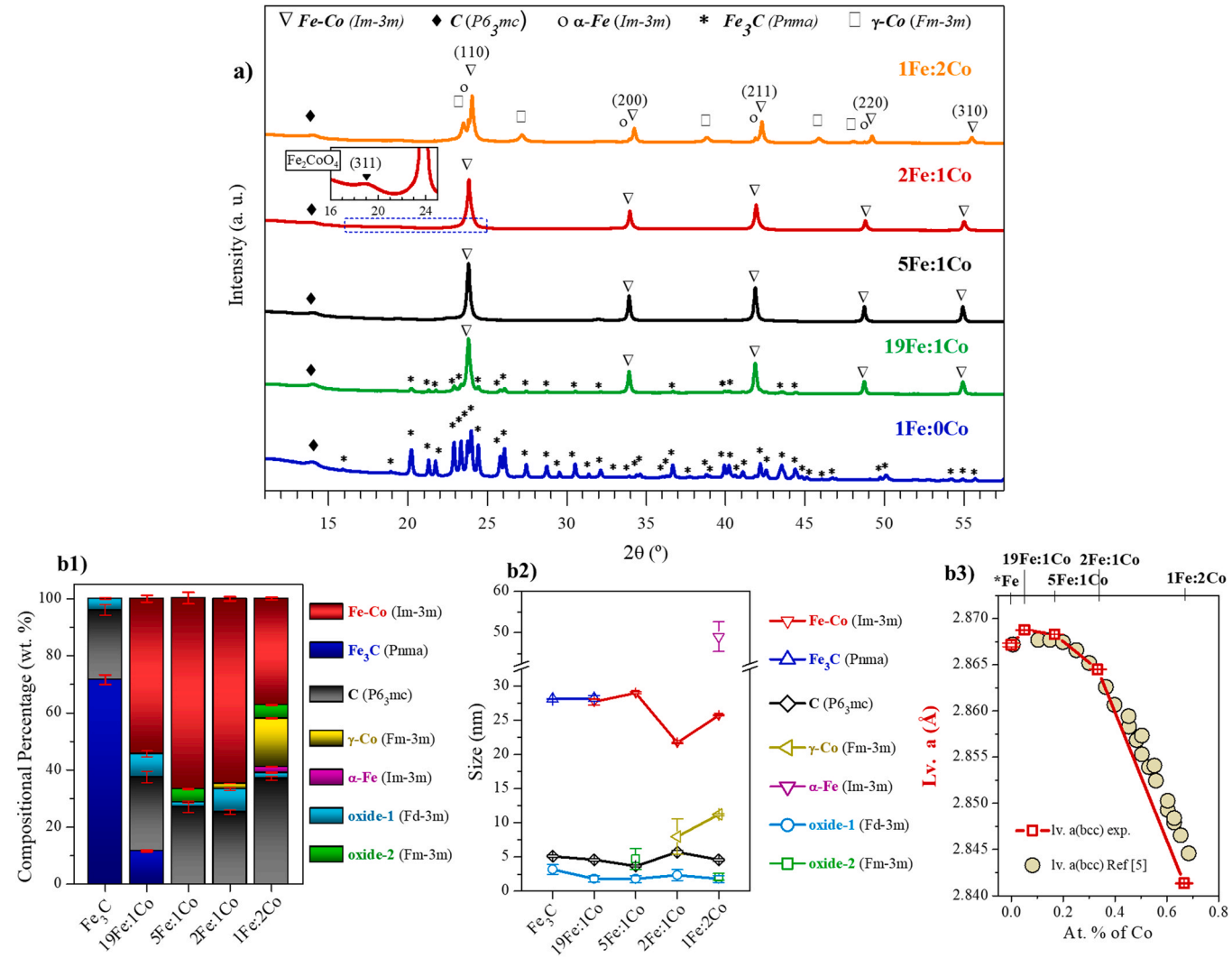

Fig. 1. (a) SXRD diffractograms for the samples synthesized with different Fe:Co ratios (1:0, 19:1, 5:1, 2:1, 1:2), and zoom insets for minority phases. (b1) Percentage composition of the phases and (b2) their crystallite size calculated from Rietveld analyses. (b3) Lattice parameter of the Fe-Co bcc phase (Im-3 m) (red) and those reprinted from [5] (yellow circles). *Fe denotes a synthesized reference-bulk-bcc-sample.

aberration corrector operated at 200 kV and equipped with a Gatan Quantum EELS detector. To compose the compositional maps, noise was removed from EELS spectrum images using principal component analysis [52]. EELS elemental maps were obtained by integrating 30–40 eV wide windows under the relevant edges after background subtraction using a power law fit. Additionally, the STEM images were processed by ImageJ software[53].

The electronic characterization, oxidation state, and local structure coordination were studied by X-ray absorption spectroscopy (XAS) at the BL22 CLÆSS beamline of the ALBA synchrotron facility in Cerdanyola del Vallès (Spain) [54]. Both X-ray absorption near-edge structure (XANES) and extended X-ray absorption fine structure (EXAFS) experiments were achieved at room temperature in transmission geometry at Fe (7112 eV) and Co (7709 eV) *K*-edges, for fabricated sample-powder-cellulose compacted films. The monochromator used in the experiments was a double Si(311) crystal. Different metal foils and oxide references were measured (see Supporting Information) and used to calibrate the energy. XAS data are analysed in accordance with standard procedures using the ATHENA and Artemis program packages [55].

The magnetic properties of the nanostructured powders were measured with a vibrating sample magnetometer (VSM) coupled to a physical property measurement system (PPMS model 6000 controller, Quantum Design). The magnetic hysteresis loops were collected at room temperature with a maximum applied magnetic field of 50 kOe.

3. Results and discussion

3.1. Structural properties and phase composition

To test the versatility of the synthetic route, five samples were synthesized with a Fe:Co molar ratio of: 1Fe:0Co, 19Fe:1Co, 5Fe:1Co, 2Fe:1Co and 1Fe:2Co. The surfactants used in the synthesis, with a molar ratio of 1ON:1OA, act synergistically constraining the particle size of primal Fe, Co or Fe-Co oxidized NPs formed at temperatures < 500 ºC (see Supporting Information). Densification temperatures up to 700 ºC ensure an effective carbothermal reduction of the Fe-Co-oxides giving rise to Fe_3C or Fe-Co-alloyed NPs embedded in a carbon matrix [56]. The surfactant concentration of 5 mmol (ON, OA) is also adjusted, optimizing the lowest presence of carbon matrix. We probe that a xerogel synthesized with 1 mmol for 1Fe:0Co, does not contain enough organic carbon to promote the reduction of oxides, and even, it impedes the formation of Fe_3C NPs, obtaining a bulk material (see Supporting Information).

Fig. 1-a shows the X-ray diffractograms for the five ratios of Fe:Co tested. The Rietveld analysis allows to extract quantitatively the compositional percentage (Figs. 1-b1), the average crystallite sizes (Fig. 1-b2) and the lattice parameters (Fig. 1-b3) of the phases included in the model for the refinement, (*see* Supporting Information). Firstly, the null content of Co (1Fe:0Co data) produces the orthorhombic phase of the intermetallic compound Fe_3C (cementite), with a crystallographic group *Pnma*. From the Rietveld refinement, the lattice parameters are a_{Fe3C} = 5.093(1) Å, b_{Fe3C} = 6.749(1) Å, and c_{Fe3C} = 4.529(1) Å, according to the literature [39,56]. Secondly, the smallest amount of Co introduced (5%, for the 19Fe:1Co sample) causes the emergence of a bcc phase (*Im-3 m*) with peaks at 2θ = 23.80, 33.91, 41.85, 48.71 and 54.93º, matching with the crystallographic planes indexed in Fig. 1-a. A remaining phase of Fe_3C is also detected, and a small lattice variation is observed (a_{Fe3C} = 5.087(1) Å, b_{Fe3C} = 6.751(1) Å, and c_{Fe3C} = 4.528(1) Å). The unit cell volume is contracted from 155.67(3) to 155.50(2) $Å^3$ in agreement with some reports that have achieved the $Fe_{3-x}Co_xC$ (*Pnma*) intermetallic-substitutional compound [40,41]. In the present case, we understand that it is not a significative difference to consider that Co is internalized in the orthorhombic structure, at least effectively, since the Fe_3C content decreases from a 72(2) % (in 1Fe:0Co) to a 11(1) % (in 19Fe:1Co), Figs. 1-b1. Hence, the Co addition acts preventing the formation of the orthorhombic $Fe_{3-x}Co_xC$ as experimental phase diagram shows for the Fe-Co alloys [5,57] and as *ab-initio* simulations predict [38].

The compositional percentage of the Fe-Co bcc alloy reaches a maximum of 68(2) % for the 5Fe:1Co sample and decreases up to 37(1) % for the 1Fe:2Co, due to the presence of secondary non-oxidized metallic phases. Its crystallite size ranges from 21 to 27 nm, very close to the 28 nm obtained for the Fe_3C phase (Fig. 1-b2). The roughly invariance of the crystalline domain size for both phases manifests that their growth might be confined by the carbon matrix influence [56,58]. Additionally, all the Fe:Co diffractograms display a peak at 2θ = 14.01º corresponding with the (002) crystallographic plane of graphite (*P6₃mc*), and lattice vector of $a_{C\text{-}g}$= 2.553(5) Å and $c_{C\text{-}g}$= 6.924(4) Å [58]. Most of the C is lost in the reduction of the xerogel removed in the form of CO_2, and the remaining forms a carbon matrix [56]. The compositional percentage of the graphite phase ranges from 24% to 36% and the crystallite size is between 4 and 6 nm. The slight increase of the composition values toward higher Co content could be correlated with the carbon diffusion, activated by the impossibility of Fe-Co to form a carbide, and hence, increasing the amount of C crystallized into graphite [59].

Furthermore, the analysis of high resolution SXRD patterns show systematically a small presence of metallic oxides in all samples, that evolves with the Co content added to the synthesis. In this sense, two cubic phases are proposed for the Rietveld analysis models: an oxide-1 (*Fd-3 m*) spinel-like; and an oxide-2 (*Fm-3 m*) face-centred cubic (fcc). The first one is present in all samples with a small crystalline size (2–3 nm, Fig. 1-b2). This oxide could be identified as Fe_3O_4 for 1Fe:0Co and with a Co-ferrite for the remaining samples. The lattice parameter of the oxide-1 for the 2Fe:1Co sample is 8.404(1) Å, close to the value of 8.388 Å reported in literature for Fe_2CoO_4 [60] instead of 8.243 Å for $FeCo_2O_4$ [61]. The zoom inset of the 2Fe:1Co diffractogram in Fig. 1-a shows the presence of the oxide-1, in agreement with the reported in similar studies for the Fe_2CoO_4 (ferrite) [28]. For more details see Rietveld refinements models in the Supporting Information. The second phase, fcc oxide-2, is only present in 5Fe:1Co and 1Fe:2Co samples with a low content of 4.5(2) % and 4.7(3) % (Fig. 1 b1). The lattice parameters computed are $a_{5Fe:1Co}$(oxide-2) = 4.297(3) Å and $a_{1Fe:2Co}$(oxide-2) = 4.232(3) Å, matching with 4.301 Å for FeO and 4.263 Å for CoO, respectively [62,63].

Despite the stability of Fe-Co alloy, others secondary non-oxidized phases are formed (Figs. 1-b1): γ-Co fcc (*Fm-3 m*) and α-Fe bcc (*Im-3 m*). Remarkably, the remaining excess of Co crystallizes into a γ-Co (fcc) with a lattice parameter of 3.559(3) Å, close to the 3.555 Å reported in literature [64]. Its compositional percentage and crystallite size increase for the highest Co amount added (1Fe:2Co). The non-presence of hexagonal-close-packaged (hcp) for Co is supported by the nanometric dimensions of all Co crystallites [65]. Additionally, a 2.1(1) % of α-Fe (bcc) with a lattice parameter of a_{Fe} = 2.867(1) Å and 49(3) nm of crystallite size is obtained for the 1Fe:2Co sample, that could come from the decomposition of Fe-Co bcc alloy at the temperatures required for the synthesis (700 ºC).

Fig. 1-b3 displays the lattice parameter of the Fe-Co alloy phase as a function of the Co percentage for the samples 19Fe:1Co, 5Fe:1Co, 2Fe:1Co and 1Fe:2Co. The sample called *Fe, was prepared with only Fe^{3+} ions and a low carbon content (1 mmol of organic surfactant). This produces a bulk sample of α-Fe with a lattice parameter of *a* = 2.8670(4) Å, according to the reported literature [66] (see Supporting information). This experimental Fe-reference sample is appropriate to correlate the evolution of the bcc structure with the Co addition. The trend observed in Fig. 1-b3 agrees with other works[5], suggesting a high accurate tunability of the alloy achieved by the followed synthesis procedure.

High resolution STEM-EELS analyses were subsequently carried out in two representative samples: 2Fe:1Co and 19Fe:1Co. Figs. 2-a1 and b1 show their low magnification annular bight field images (ABF) respectively, with NPs embedded in a carbon matrix. The NPs exhibit uneven spherical shapes with a PSD represented in Figs. 2-a2 and b2. For both samples, a bimodal distribution is detected which has been fitted by two Gaussian curves. The 2Fe:1Co PSD has maxima at 10.4(1) and 21(1) nm their full width high maximum (FWHM) values are 5.9(1) and 19.9(1) nm, respectively. This fact could be due to the low presence of carbon matrix in 2Fe:1Co, which allows for the NPs agglomeration[67]. Curiously, some NP sizes are double by pairwise coalescence. For the 19Fe:1Co sample, two maxima are located at 24(7) and 45(1) nm. Probably, a primal PSD distribution centered in ~10 nm evolved towards its complete transformation into ~20–25 nm sizes and, subsequently, ~40–50 nm. Interestingly, the 21(1) nm PSD maximum inferred from STEM images is consistent with the 21.7(1) crystallite size calculated by Rietveld refinement for 2Fe:1Co. Likewise, the PSD maximum located at 24.7(5) nm is close to the Rietveld value of 27.7(5) nm for 19Fe:1Co (Table 1). Therefore, the NPs can be considered as single-crystals.

Figs. 2-a3 and b3 show high angle annular dark field (HAADF) images of a single NP of 2Fe:1Co and 19Fe:1Co respectively, confirming a core/shell structure for both samples. A zoom of the region marked with a yellow square in Figs. 2-a3 is presented in Figs. 2-a4, showing the atomic columns of both core and shell contributions. Two FFTs are represented in the insets 1 (shell) and 2 (core). The shell is consistent with the (220) and (20$\bar{2}$) Miller indexes of a *Fd-3 m* spinel structure (zone axis, ZA = [1$\bar{1}$1]), corresponding both with an interplanar distance (d) of 0.27(7) nm. Similarly, the FFT core displays the crystallographic planes (110) and (0$\bar{1}\bar{1}$) (ZA = [1$\bar{1}$1]), for an *Im-3 m* bcc structure, giving a d = 0.21(2) nm. Therefore, a Fe-Co-alloy/(Fe_2CoO_4) morphology is identified for the 2Fe:1Co sample and agrees with the presence of the oxide-1 in the XRD (Fig. 1, *inset*). For the 19Fe:1Co sample, the zoom of the shell region indicated with a yellow square in Figs. 2-b3 shows the (002) planes of graphite with a d = 0.37(5) nm. Likewise, Figs. 2-b4 displays a zoom of the core NPs shown in Figs. 2-b3. The FFT of the inset displays the (200) and (010) Miller indexes of a *Pnma* structure (Fe_3C), with d = 0.26(2) and 0.70(3) nm, respectively. As a result, the 19Fe:1Co sample consists in Fe_3C/graphite NPs embedded in a carbon matrix.

The crystalline size, lattice parameters, and interplanar distances obtained from Rietveld and STEM analyses are summarized in Table 1 for 2Fe:1Co and 19Fe:1Co samples, obtaining similar values coming from both characterization techniques.

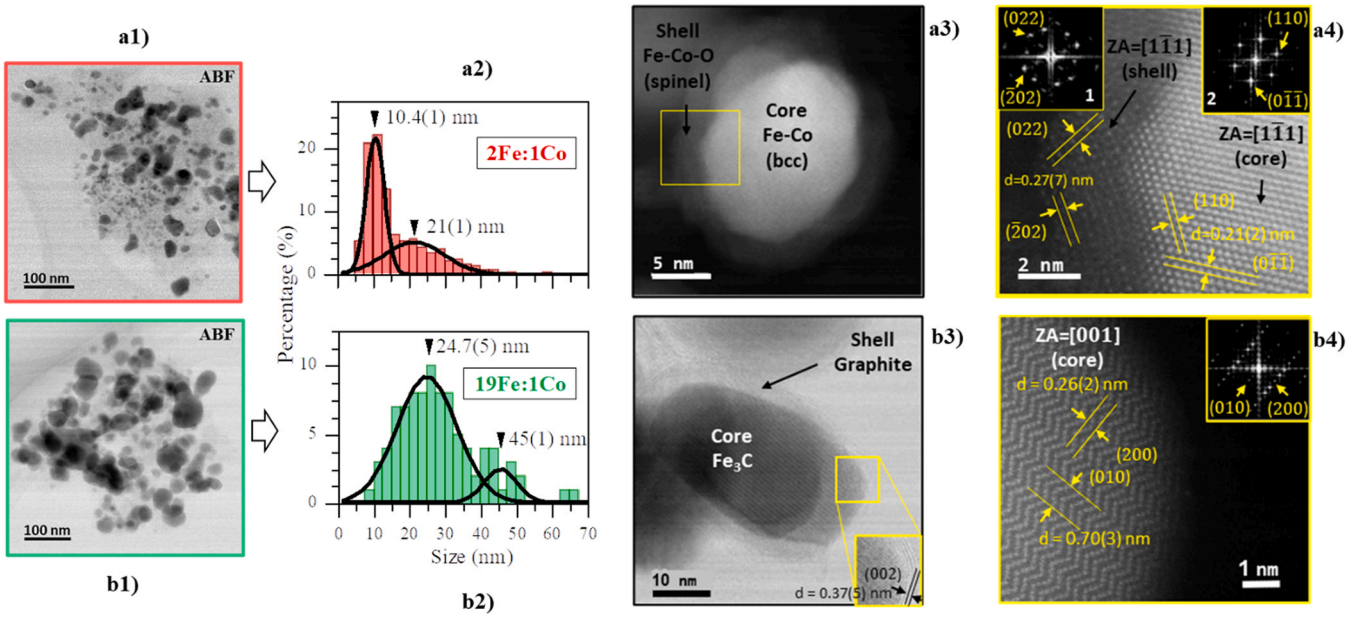

Fig. 2. *(a) 2Fe:1Co sample:* (a1) low magnification ABF image for Fe-Co (bcc) alloyed NPs embedded in a carbon matrix, (a2) PSD, (a3) HAADF image of a Fe-Co/Co-ferrite core/shell NP, and (a4) HAADF zoom of the region indicated with a yellow square in (a3). Insets 1–2 of (a4) display the fast Fourier transform (FFT) of the shell (Fe_2CoO_4) and core (Fe-Co) respectively. *(b) 19Fe:1Co sample:* (b1) low magnification ABF image for Fe_3C (cementite) NPs embedded in a carbon matrix, (b2) PSD, (b3) ABF image of a Fe_3C/graphite core/shell NP with a zoom evidencing the graphite shell, and (b4) zoom of the Fe_3C core NP of (b3) with its FFT showed in the inset.

The composites are also studied simultaneously with EELS to quantitatively analyse the local composition of the core/shell nanostructures. Figs. 3-a1-a5 show the resulting merged elemental compositional map for the sample 2Fe:1Co, assigning the intensities of O (*K*-edge, blue colour), Fe ($L_{2,3}$-edge, green colour) and Co ($L_{2,3}$-edge, red colour).

A confined oxygen predominance in the shells and a Fe-Co (bcc) alloy in the cores is inferred from the images. Analogously, the C, Fe, and O signals evidence a core/shell NP surrounded by a carbon matrix (Figs. 3-a2), consistent with STEM results (Fig. 2). The top of Figs. 3-a3-a5 corresponds to a single representative NP of 2Fe:1Co sample, showing the signal intensities of O *K*-edge, Fe and Co $L_{2,3}$-edges, respectively. At the bottom, compositional atomic percentage profiles measured across the particle are displayed corresponding to the area marked with a yellow rectangle. The integral of the histograms for Fe and Co elements gives an average Fe:Co ratio in the core/shell NP of 2:1, in agreement with the 2Fe:1Co ratio introduced in the synthesis. Regarding the shell, the average atomic composition percentages measured give values of 55% of O, 34% of Fe, and 11% of Co; close to the 57% of O, 29% of Fe and 14% of Co for the stoichiometric Co-ferrite Fe_2CoO_4. This result agrees with the spinel-oxide for the 2Fe:1Co sample evidenced in Fig. 1-b2. A thickness of 3 nm is inferred for the shell from Figs. 3-a3 which is also compatible with the 2.3(5) nm crystalline size calculated by Rietveld.

Finally, Fig. 3-b represents the compositional map for the sample 19Fe:1Co. Similarly, core/shell NPs are found surrounded by a carbon matrix but, in this case, the surface of the NPs exhibits a lower oxidation degree and a homogeneous C capping, consistent with the graphite shells observed in the STEM images (Figs. 2-b3). The regions marked with orange rectangles (denoted with 1, and 2) suggest that the 19Fe:1Co sample could be constituted by two types of NPs: Fe_3C (rectangle 1) and Fe or Fe-Co (rectangle 2) NPs as it is obtained by Rietveld analysis (Fig. 1). The low Co content hinders its detection in this sample.

Summarizing, here we report one of the most homogeneous and lowest ratios between core-size and shell-thickness, as compared to some other reported Co-ferrite capped Fe-Co cores [7,28,33,68], along with a good degree of tunability of the core alloys.

3.2. Electronic properties

Trying to understand the overall average degree of oxidation of the whole synthesized Fe:Co samples, and the contribution of the oxides predicted by Rietveld analysis and corroborated by STEM-EELS, a XAS analysis was carried out at the Fe,Co *K*-edges. Figs. 4-a1 and b1 show the experimental XANES spectra for samples varying the Fe:Co ratio along with metallic references of Fe and Co foils, respectively. In addition, the oxide references: CoO, Co_3O_4, FeO, α-Fe_2O_3 and Fe_3O_4 are included in the Supporting Information. At the

Table 1
I): Crystallite sizes and lattice vector inferred by Rietveld refinement. II): Average NP size (diameter) and lattice parameters computed by the STEM analyses.

	I) Rietveld Analyses	
Sample	Crystalline size (nm)	Lattice vectors (Å) - "core/shell"
19Fe:1Co	27.7(5)	$a_{(Pnma)}$ = 5.093(1), $b_{(Pnma)}$ = 6.749(1) / $c_{(P63mc)}$ = 6.924(4)
2Fe:1Co	21.7(1)	$a_{(Im\text{-}3\,m)}$ = 2.86448(3) / $a_{(Fd\text{-}3\,m)}$ = 8.404(1)
	II) HR-STEM Analyses	
Sample	Particle size (nm)	Lattice vectors(Å) - "core/shell"
19Fe:1Co	24.7(5), 45(1)	$a_{(Pnma)}$ = 5.2(4), $b_{(Pnma)}$ = 7.0(4) / $c_{(P63mc)}$ = 7.2(5)
2Fe:1Co	10.4(1), 21(1)	$a_{(Im\text{-}3\,m)}$ = 2.9(4) / $a_{(Fd\text{-}3\,m)}$ = 7.6(9)

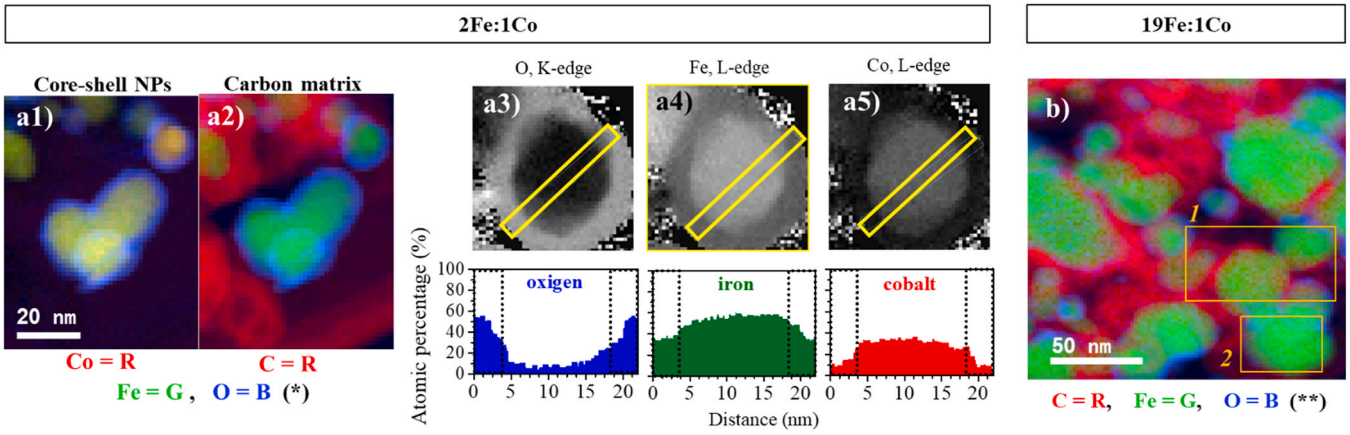

Fig. 3. (a1-a2): Coloured images generated by the superposition of the elemental compositional maps of the 2Fe:1Co sample by the coding: {Co (red), Fe (green), O (blue)} and {C (red), Fe (green) and O (blue)} respectively. (*) denotes coding colours common for both images. (a3-a5): Compositional atomic percent maps for a single 2Fe:1Co NP based on the analysis of the O *K*-edge, Fe $L_{2,3}$-edge, and Co $L_{2,3}$-edge, respectively. At the bottom of each corresponding histogram, the composition is shown the profiles extracted from the yellow rectangles. (b) Coloured image by the overlay of the elemental compositional maps of 19Fe:1Co sample: {C (red), Fe (green), O (blue)} (**, no Co detected). Orange rectangle 1 shows Fe-C NPs corresponding with Fe_3C NP, and orange rectangle 2 for Fe rich NP associated with α-Fe.

Fe *K*-edge (Figs. 4-a1), the absorption spectra of all samples are very similar to that of Fe reference film and correspond to the bcc Fe-Co structure. The first inflection point of the main Fe *K*-absorption edge of samples falls around 7112 eV and is related to Fe quadrupole 1 s → 3d transitions [69]. Its intensity is lower than that of α-Fe foil indicating the structural disorder induced by the Co ions into the Fe structure. The following resonances change in intensity for the samples, suggesting that the Co addition modifies the coordination of the Fe-bcc atoms. At the Co *K*-edge (Figs. 4-b1), the absorption signal can also be associated mainly with a Fe-Co bcc structure, against the α-Co reference foil (hcp), where the absorption edge is around 7709 eV. In this case, the main Co *K*-absorption edge is associated with 1 s → 4p transitions and its intensity is lower compared to that of Co foil, indicating a structural disorder induced by Fe ions. The changes in the main post-edge resonances are more pronounced among samples synthesized with the increasing of Co proportion. This suggests the existence of modifications in the

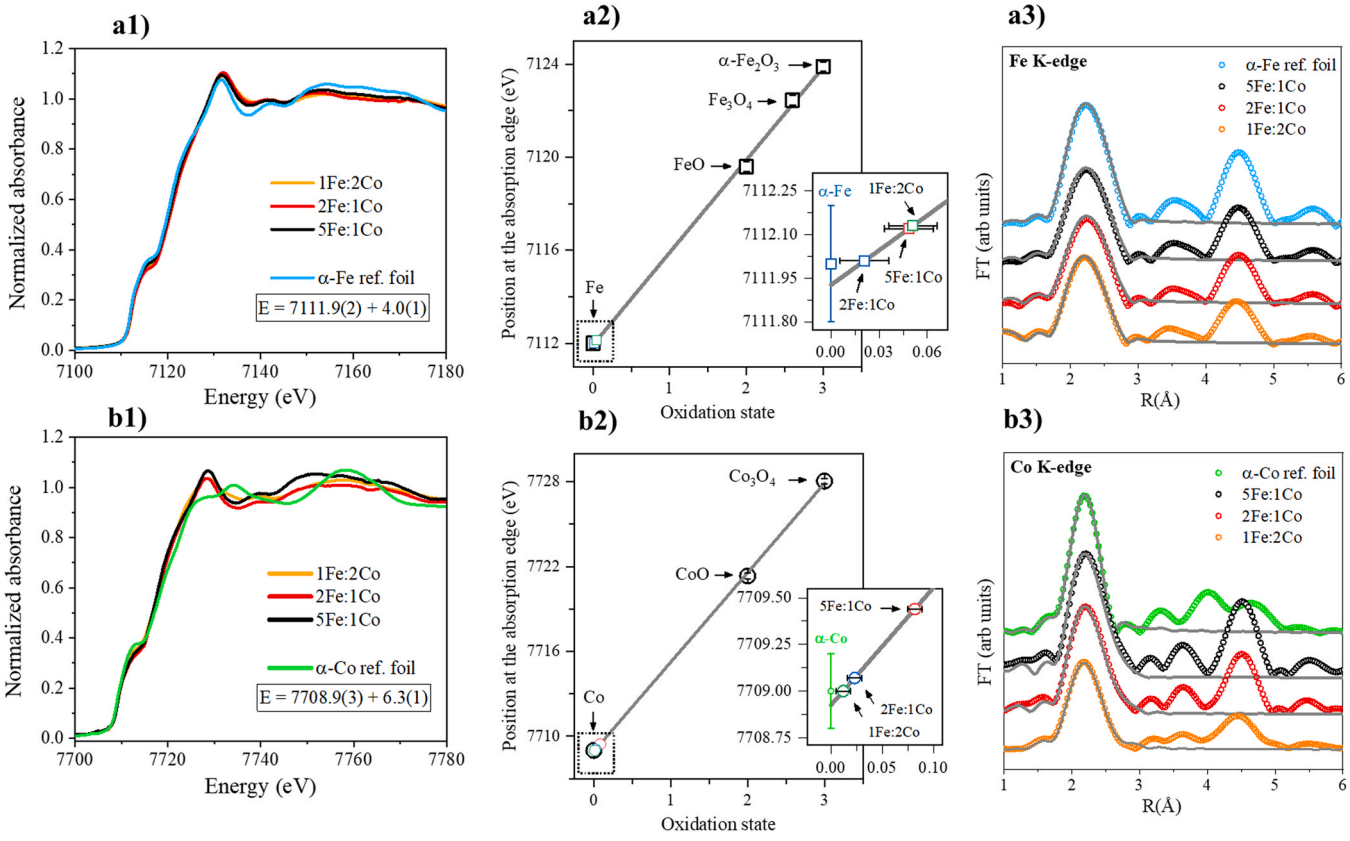

Fig. 4. XANES spectra of samples and metallic reference foils: *K*-absorption edges of Fe (a1) and Co (b1), and the energy value of *K*-edge of foils at the horizontal text box. Linear fits for the position of the *K*-absorption edges with the oxidation state for different commercial metal-oxide reference compounds: *K*-edges of Fe (a2) and Co (b2), black squares and circles, respectively. The position of *K*-edge is displayed in the zoom insets of the dotted squared region. Fourier transform modulus of the EXAFS spectra for (a3) Fe *K-edge* and (b3) Co *K-edge*. Fitting-simulations of the samples (continuous lines) are compared with the Fe and Co foils measured.

coordination of the Co atoms by the compositional changes and the γ-Co emergence in 2Fe:1Co and 1Fe:2Co samples (Figs. 1-b1).

The overall oxidation state of the absorbing atoms in each sample is determined from the linear relationship between the *K*-absorption edge energy value and the average oxidation state of the atoms of the metal-oxide references measured [70–72]. Figs. 4-a2 and b2 show both linear fits for the commercial references employed. The oxidation state of the Fe and Co cations is obtained from the linear fit at each respective absorption edge. The zoom insets of Figs. 4-a2 and b2 shows that the main absorption edge for the samples is very close to that of α-Fe and α-Co reference foils respectively, indicating that the valence is close to 0 for both the Fe (< 0.06, [70,72]) and the Co (< 0.1, [73,74]) cations for all samples. In both cases, the small variations could be both related to a different cation-coordination environments of Fe-Co bcc alloy and the slight oxidation of the Fe and Co atoms into the samples. However, such minimal changes indicate a low presence of oxides in the samples.

The short-range order of cations is analysed as a function of the Fe:Co ratio. Figs. 4-a3 and b3 display the modulus of the Fourier transform (FT) of the EXAFS signal at the Fe and Co *K*-edges for the samples along with the Fe and Co foils, respectively. The fitting at the Fe *K*-edge considers two shells (Fe-Co and Fe-Fe), considering the interaction of Fe absorbing atoms with both Co and Fe neighbours. Analogously at the Co *K*-edge, two shells are also considered: Co-Fe and Co-Co interactions. Table 2 displays the EXAFS results obtained from the fitting of samples and reference foils for: the coordination number *N*, the interatomic distance *R* and the Debye-Waller (DW) factors σ^2, used as free parameters.

On the one hand, one peak containing the two fitting shells at the Fe *K*-edge EXAFS signal (Figs. 4-a3) is clearly identified for all samples showing a similar signal to that of the Fe foil. The first one is located at ~2.47 Å (Fe-Co bonds) and the second one is at ~ 2.84 Å (Fe-Fe) (see Table 2). On the other hand, it is found at the Co *K*-edge EXAFS signal (Figs. 4-b3) a first shell located at ~2.47 Å (Fe-Co) (similar value than at the Fe *K*-edge), and the second one is at ~2.85 Å (Co-Co). No longer features of the Co foil are observed for all samples at long distances, and the new contribution is associated with the Co-Fe bcc alloys.

In detail, the most significant changes in k^3-weighted EXAFS spectra of the K-edges of the Fe and Co correspond to the intensity of two shells fitted, which may be attributed to the coordination of cations and the DW factor (structural disorder). Respect to the coordination number, a decrease in both two shells obtained for each K-edge (Fe and/or Co) as the Co amount increases. Whereas the DW factors are similar in all samples regardless of the shell and the *K*-edge considered, except for the 1Fe:2Co sample. For this latter, the DW factor decreases in the Fe-Fe and increases in the Co-Co shells respectively, probably due to the large amount of Co in the structure and the rising of the γ-Co phase. Finally, a decrease of the radial distribution is identified at both shells and *K*-edges as the Co quantity increases. The lowest values are obtained for the sample 1Fe:2Co, as is reflected in Fig. 1-b3.

Summarizing, these findings corroborate the formation of Fe-Co bcc alloys in the analyzed samples, maintaining the coordination ratio in both shells (8:6 for the bulk). Nevertheless, a shortening of some neighbour distances induced by the incorporation of Co in the Fe lattice is identified, which increases with the Co amount. In addition, no shell related to any Fe or Co oxides are detected.

Table 2
Parameters obtained from the EXAFS fittings for two shells proposed at each absorption edge.

Sample	Absorption edge	Shell	N	R (Å)	DW (Å^2)
Fe foil	Fe *K*-edge	Fe-Fe	8	2.464(8)	0.0054(2)
		Fe-Fe	6	2.84(1)	0.0070(2)
Co foil	Co *K*-edge	Co-Co	12	2.501(1)	0.0053(3)
5Fe:1Co	Fe *K*-edge	Fe-Co	6.5(2)	2.470(3)	0.0056(3)
		Fe-Fe	4.9(3)	2.836(5)	0.0077(6)
	Co *K*-edge	Co-Fe	6.2(3)	2.467(3)	0.0052(7)
		Co-Co	5.1(2)	2.856(8)	0.0054(9)
2Fe:1Co	Fe *K*-edge	Fe-Co	6.1(3)	2.467(8)	0.0058(2)
		Fe-Fe	4.6(2)	2.832(6)	0.0074(3)
	Co *K*-edge	Co-Fe	5.5(4)	2.470(9)	0.0052(2)
		Co-Co	4.2(3)	2.849(6)	0.0060(6)
1Fe:2Co	Fe *K*-edge	Fe-Co	6.1(3)	2.458(4)	0.0055(5)
		Fe-Fe	4.6(3)	2.825(9)	0.009(1)
	Co *K*-edge	Co-Fe	4.7(3)	2.46(6)	0.0054(2)
		Co-Co	3.5(4)	2.844(9)	0.0089(6)

3.3. Magnetic properties

Fig. 5-a shows the hysteresis loops for samples with different Fe:Co ratios. The values of coercive field (H_C) and saturation magnetization (M_s) are summarized in Table 3 and represented in Fig. 5-b as a function of atomic percentage of Co added into the synthesis.

The synthesized reference bulk-sample (*Fe bcc in Table 3) prepared with only Fe^{3+} and a low carbon content (1 mmol) has a value of 215 emu/g, very close to 217 emu/g reported for α-Fe [77]. The M_s of 1Fe:0Co sample composed by Fe_3C nanoparticles embedded in a carbon matrix, is 80 emu/g. This value is lower than the bulk Fe_3C one (~140 emu/g) [39] due to the presence of non-magnetic phases such as the carbon matrix, which contribute to the mass renormalization of the magnetic signal. However, under these premises, it is at least 40% superior to others Fe_3C NPs@carbon-matrix systems [78,79]. Regarding the Co-based samples, this effect is also observed, showing competitive values for Fe-Co based systems (Table 3).

Interestingly, Fig. 5-b shows that the small addition of Co (19Fe:1Co) increases the M_s correlated with an abrupt emergence of a 54(1) % of the Fe-Co bcc phase as is reflected in Figs. 1-b1. This abrupt emergence is accompanied by a decrease of Fe_3C orthorhombic phase (with lower M_s). It is well known that, despite the elevated M_s of the Fe bcc phase (~ 218 emu/g), the addition of Co to form Fe-Co bcc alloys increases the M_s with a maximum of 240 emu/g at ~25–30% of Co [5]. In our work, the 5Fe:1Co sample, with Fe-Co bcc alloy as a predominant phase, shows the highest M_s (137 emu/g). Lower M_s are observed as Co addition increases, mainly due to the occurrence of the secondary γ-Co fcc phase (M_s(γ-Co) = 165 emu/g [80]), especially in the 1Fe:2Co sample. However, the compositional percentage of the phases in Figs. 1-b1 allows a $M_s$renormalization (neglecting the oxides contributions), giving more realistic increased values for the Fe-Co bcc phase (see red M_s^{bcc} curve in Fig. 5-b). M_s^{bcc} lies around 200 emu/g finding a maximum between 15% and 35% of Co concentration, consistent to the 25–30% reported in literature [5,24]. Finally, the renormalized values (~200 emu/g) differ from such reported for pure Fe-Co alloys (~240 emu/g) by the possible contribution of other C-O or C-N-O amorphous phases present in the matrix that could be not reflected in Rietveld analysis.

The evolution of the H_C values displayed in Fig. 5-b is highly remarkable. A significative increase is observed in the Fe-Co bcc samples ranging from 385 to 490 Oe when they are compared to the 39 Oe of the *Fe synthetized sample (typical value for the α-Fe soft magnetic material). The high coercivity values are not far from those measured in the 1Fe:0Co sample (Fe_3C; H_C=585 Oe), which is considered in literature as a semi-hard magnetic phase. Here, the origin of the magnetic hardness comes from its orthorhombic magnetocrystalline anisotropy [2,56]. In the same line, the 19Fe:1Co sample exhibits an incremented value of 490 Oe consistent with the presence of the orthorhombic Fe_3C phase (Figs. 1-b1).

To unravel the origin of such augmented H_C in Fe-Co bcc alloys, firstly, we estimate the magneto-crystalline anisotropy constant, *K*, for the samples with predominant bcc contents (5Fe:1Co and 2Fe:1Co), considering that the magnetic response comes from the

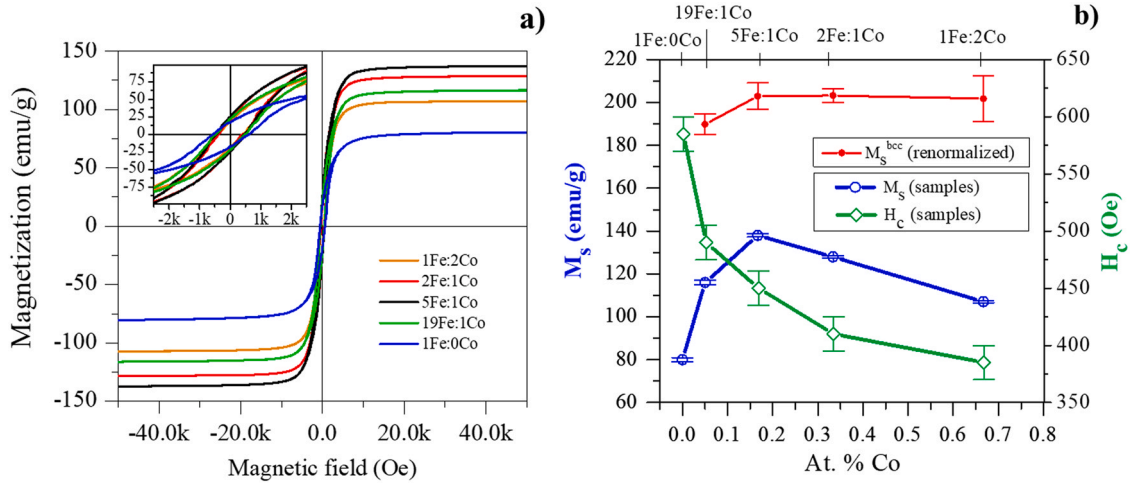

Fig. 5. (a) Magnetic hysteresis loops taken at 300 K for the different Fe:Co ratios and the respective zoom inset. (b) Saturation magnetization (blue), and coercive field (green) dependencies as a function of the Co atomic percentage in the samples. The red data correspond to the M_s^{bcc} renormalized values, *i.e.* the $M_s$for pure Fe-Co bcc phase for which C-matrix and other phases obtained by Rietveld refinement are not considered in the total moment measured normalization.

Table 3
Summary of the magnetic parameters for samples with different Fe:Co ratio and an additional *Fe bcc (of α-Fe) synthesized reference sample.

at% of Co	Sample	M_s ± 1 (emu/g)	M_s^{bcc} (emu/g)	H_C ± 15 (Oe)	K (kJ/m^3) at 300 K
0	*Fe	215	-	39	46.8 for pure Fe[75]
0	1Fe:0Co	80	111 ± 3	585	155 for pure Fe_3C[76]
5.0	19Fe:1Co	116	190 ± 5	490	-
16.7	5Fe:1Co	137	203 ± 6	450	29.0 [this work]
33.3	2Fe:1Co	128	203 ± 3	410	26.4 [this work]
66.7	1Fe:2Co	107	201 ± 11	385	-

cores (*i.e.*, neglecting the presence of magnetic oxides and graphite). To do that, a law-approach-to-saturation fitting method (LAS) is used (see Supporting Information). Assigning for the *Fe experimental reference sample the well-known value reported in the literature of K = 46.8 kJ/m^3 for α-Fe at 300 K [75], LAS method gives 29.0 and 26.4 kJ/m^3 for the K constant of 5Fe:1Co and 2Fe:1Co samples, respectively (Table 3). These calculated K values decrease with Co content, and they are lower than those ones related to the *Fe sample. The addition of Co atoms modifies the crystal field surrounding a particular Fe atom relative to that of a bcc environment containing only Fe atoms. This change directly affects the spin-orbit interaction responsible of the magneto-crystalline anisotropy energy, in this case promoting a decrement, as is reported in the literature for $Fe_{65}Co_{35}$ ($K \sim 20$ kJ/m^3) [4,8]. Despite being our K values obtained slightly higher than those one reported, a correct ratio between K_{*Fe} and K_{Fe-Co} is maintained, thus providing an adequate estimation of the anisotropy constant values.

Once the magneto-crystalline constants have been estimated, the measured coercivities could be analyzed. Theoretically, the coercive field associated with isolated and homogenous magnetized NPs is given by the limit of the magneto-crystalline anisotropic field, $H_K = \frac{2K}{\mu_0 M_s}$; *i. e.* $H_C \geq H_K$. Computing H_k for 1Fe:0Co and 2Fe:1Co samples with the K estimated values (Table 3) and the referenced M_s bulk values (140 and 240 emu/g respectively), results in a H_K(1Fe:0Co) = 2840 Oe and H_K(2Fe:1Co) = 280 Oe. In the case of 1Fe:0Co, the H_K computed (2840 Oe) is superior to the experimental H_C (585 Oe). Regarding this approximation applied to real magnetic systems, an overestimation of more than one order of magnitude is typically retrieved. This fact is usually known as the Brown's paradox and it is resolved considering that the defects or nanoscale imperfections reduces the H_K to an effective H_C [81]. In this context, a remarkable opposite behavior is observed in our bcc Fe-Co NPs. The measured H_C values (450 and 410 Oe for the 5Fe:1Co and 2Fe:1Co samples, respectively), are far from the H_K=280 Oe calculated.

To understand the origin of such unusual behavior, a state-of-art of the coercive field in bcc Fe-Co nanosized systems is reviewed as a function of the particle size (Fig. 6). The data are also classified as a function of the synthesis method used; that is by chemical methods (acid media and basic media (polyol) approaches), and physical methods (other methods). Generally, for large scalable chemical synthesis, polyol methods seem to be adequate to synthesize larger NP sizes than the acid media sol-gel-macromolecules approaches [34,35], being the latter the group in which our work is framed.

Roughly speaking, two main regions can be distinguished in Fig. 6 corresponding to the *standard H_C region* (full-filled symbols) and *enhanced H_C region* (empty or star symbols). The *standard H_C region* reflects more clearly the transition between multidomain (MD) to single domain (SD) behaviors, with a H_C maximum located at ~20 nm NP size. Discrepancies from the theorized laws for coercivity size dependence ($H_c \sim -\frac{1}{l^{3/2}}$ for SD and $H_c \sim \frac{1}{l}$ for MD, being l the physical size [82]), manifest that each system can be influenced by stress, geometry, particle interactions, presence of other phases, etcetera. These factors may also modify the effective magnetic anisotropy, and the associated coercive field, undrawing the predicted trend theory for MD and SD behaviors. Based on this review, we conclude that our composites with average NP sizes centered around ~21 nm are mainly magnetic single domain.

Considering now the *enhanced H_C region*, H_C values of a few hundred Oe are achieved for sizes higher than 20 nm. Surprisingly, we observe a huge increase near the MD-SD transition. Particularly, the NPs embedded within carbon matrices (star-symbols in Fig. 6) show a higher H_C than to other particle systems. This fact could not be associated with the intrinsic NP shape anisotropy because such NPs systems are generally spherical-like and no geometric order is present among them. To the best of our knowledge, only for long-

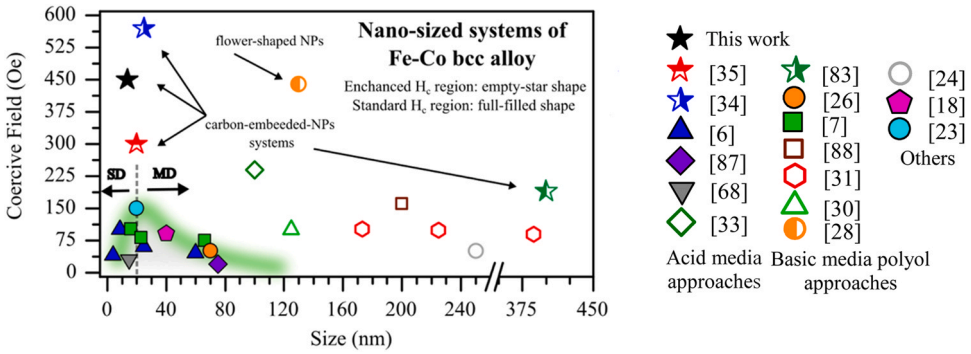

Fig. 6. Review of the state-of-art of some Fe-Co bcc systems with NP geometry representing the coercive field as a function of the NP size (diameter). Two regions are distinguished: *enhanced coercive field* (empty or star symbols) and *standard coercive field* (full-filled symbols) [87,88].

chains bcc Fe-Co NPs (extrinsic shape anisotropy), H_C ~ 765 Oe was reported by J. Lui et al. [8], where the long-chains are achieved by a magnetic alignment during the sputter-based gas-condensation synthesis.

Specifically, the only common scenario for the systems located at the *enhanced H_C region* (in particular the systems indicated with a star symbol [34,35,83] and *this work*), is the existence of a carbon matrix embedding NPs and a core/shell morphology. It is well known that the carbon matrix can play a key role on the magnetic interactions between NPs. For example, in systems with tuned interparticle distances, M. Woińska et al. [84] reported a progressive increment in H_C as the distance between them increased (*i.e.* as the magnetic interactions are weakened). In turn, the magnetic shells can also harden the magnetic response of ferromagnetic cores by exchange interactions. To evaluate the roll of these two factors, low temperature magnetic measurements are carried out (Fig. 7).

Figs. 7-a1 shows the magnetization as a function of temperature measured for the 5Fe:1Co and 2Fe:1Co samples, both after zero field cooled (ZFC) and field cooled (FC) with 100 Oe applied and field cool field. The FC curves displays a nearly constant behavior typical of magnetically interacting NPs, as opposed to the increasing magnetization value with decreasing temperature typically found in systems with isolated NPs [85]. However, the high NPs density embedded in the diamagnetic carbon matrix should not lead to a significatively increment of H_C. Thus, we conclude that the enhanced H_C must come from the exchange interaction between the Fe-Co core and the Fe_2CoO_4 shell found in our samples. In this context, the Fe_2CoO_4 possesses a constant magneto-crystalline anisotropy value of K = 37 kJ/m^3 with a M_s ~ 48 emu/g [86], obtaining a high H_K ~2700 Oe. Therefore, the magnetically hard nature of the shell in our system hardens the soft Fe-Co alloy, obtaining an optimized spring-magnet system. A hysteresis loop is collected at 5 K for the 2Fe:1Co sample to corroborate if there are uncoupled magnetic contributions (Fig. 7-b). Interestingly, no plateaus ("bee waist") are observed as happens in multi-magnetic-phases systems, specially at low temperatures[48]. Therefore, a highly effective coupling between core and shell causes a simultaneous collective behavior for the magnetization reversal in each NP, demonstrating an effective spring-exchange interaction. This effect has been recently reported for Fe_2CoO_4/FeO/FeCo spring magnet composites with a high H_c ~ 800 Oe, and M_s ~ 120 emu/g [48]. Although they obtain a higher coercivity, probably due from the exchange interaction of the three materials, the renormalized M_s is much higher in the systems obtained in this work (Table 3).

Coming back to the Figs. 7-a1, contrary to what would be expected from isolated 10 nm diameter NPs with K ~25 kJ/m^3, the trend of MZFC does not show a clear blocking temperature (T_B) confirming the ferromagnetic behavior observed at 300 K (Fig. 5-a). Conversely, a nearly continuous increase in magnetization with temperature is observed, characteristic of an assembly of blocked particles with randomly oriented easy axes. The magnetization of each particle is gradually unblocked by thermal activation

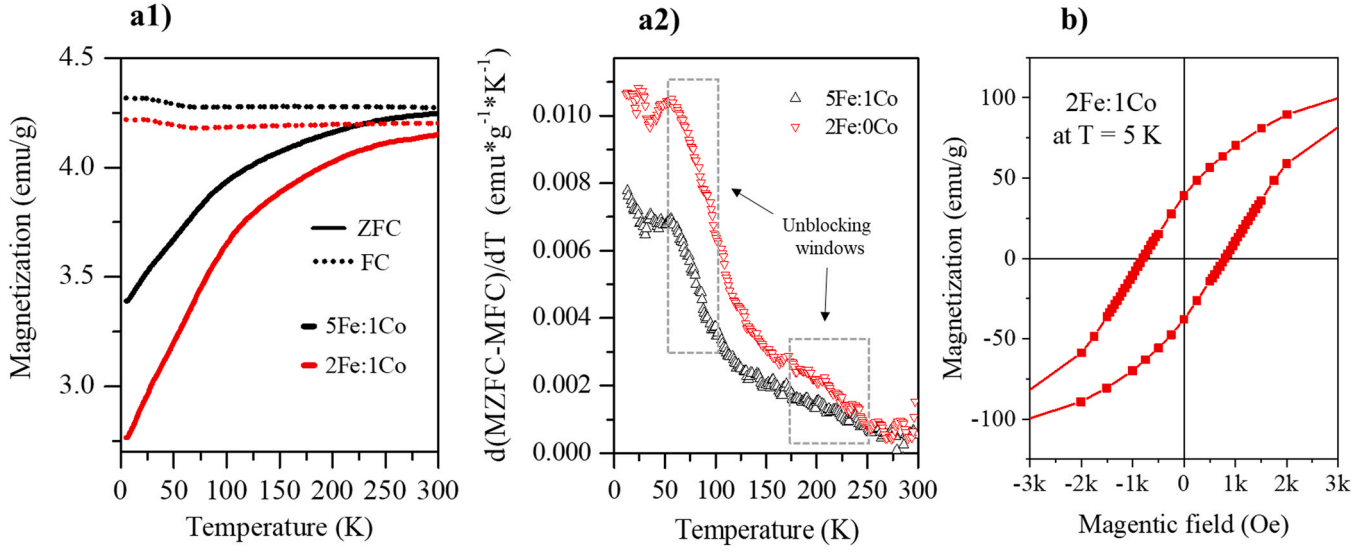

Fig. 7. (a1) ZFC (solid lines) and FC (dash lines) magnetization and (a2) first derivative difference as a function of temperature for 5Fe:1Co (black color) and 2Fe:1Co (red color) samples. (b) Hysteresis loop acquired at 5 K for the 2Fe:1Co sample.

(depending on their size) and aligned with the magnetic applied field, contributing to increase the net magnetization. Despite this, the d(MZFC-MFC)/dT curves evidence two unblocking thermal-assisted regions located at 50–100 K and 175–250 K (marked by squares in Figs. 7-a2). These intervals are understood as a reminiscence of the superparamagnetic (SP) transition of some isolated Fe-Co NPs. That is, the whole of the NPs may remain magnetically coupled among them due to their agglomeration and thermally stabilized by the shell-exchange, and hence showing hysteresis and remanence still up to 300 K. The critical sizes for the thermally assisted magnetization transition of isolated NPs could be estimated relating the thermal energy and the anisotropy barrier energy as $25K_BT = KV$ (with V the NPs volume). The clearest unblocking window (50–100 K), throws an interval of NPs diameter of $d \sim$ 11–14 nm (both for 5Fe:1Co and 2Fe:1Co). These values match perfectly with the PSD maximum represented in Figs. 2-a2 and confirm a good estimation of the K values. In turn, the other thermal window (175–250 K), corresponds to $d \sim$17–19 nm indicating the superparamagnetic transition of isolates particles with higher sizes and reflecting the uneven PSD contribution as is predicted by HR-TEM.

To conclude, the review of the state-of-art for the Fe-Co alloyed systems presented in Fig. 6 reveals that the hardening of the H_c may result from a soft/hard spring-exchange interaction, particularly in the reports indicated by a star symbol with a core/shell morphology NPs. As a result, the main function of the carbon matrix is the particle size confinement at the nanoscale and the interparticle magnetic interactions through the carbon encapsulation play a less fundamental roll. The novel easy-handle, low cost, reproducible, and scalable synthesis method here presented, is a promising route for obtaining spring magnet core/shell NPs composites with semi-hard magnetic properties. Thus, we believe that this simple approach could be extended easily to other magnetic NPs alloys embedded in a carbon matrix with potential applicability.

4. Conclusions

In this work, we present an exploration of a synthesis approach based on a sol-gel macromolecule-surfactant method for several xerogels synthesized with different metal cations ratios of Fe^{3+} and Co^{2+} from 1:0, 19:1, 5:1, 2:1 and 1:2 (Fe:Co). The Co addition impedes the formation of the orthorhombic *Pnma* Fe_3C structure but allows a perfect modulation of the emerged Fe-Co bcc alloy phase that is reflected on its lattice parameter dependence with Fe:Co ratio. A small amount of spinel-like oxide and graphite phases are found in every sample. The synthesized materials are constituted by Fe-Co NPs embedded in a carbon matrix with a bimodal PSD with maxima at ∼10–20 nm. They are mainly single-crystal with a core/shell geometry of Fe-Co alloy/Co-ferrite. The electronic properties of the Fe-Co NPs analyzed reflect a highly metallic character, with an oxidation state close to 0 (< 0.06 for Fe and < 0.1 for Co). The magnetic properties correspond to a semi-hard magnetic carbon composite, displaying an elevated M_s of ∼137 emu/g and an enhanced H_C of ∼450 Oe. The hardening is produced by a spring exchange effect between the soft FM core and the semi-hard FM shell, combined with a particle size close to the magnetic single domain behavior for the most of them. The low percentage of Co-ferrite detected (∼ 8%), compared with other investigations, indicates a very effective shell exchange coupling. The spring-exchange stabilizes NPs together with their magnetic interparticle interactions, allowing a FM behavior even at 300 K. Furthermore, a comparative magnetic analysis with the state-of-art is carried out for our magnetic composites with an enhanced coercive field and preserving an elevated saturation magnetization values that could offer multifunctional properties.

CRediT authorship contribution statement

A. C-S., J. L.-S., E. N., P. M., and N. C. conceived the work and coordinate the research. A. C. and I-S. prepared the samples. A. C-S, J. L-S, A. S., G. G, and M. V. carried out the structural characterization. A. C., E. N. and A. H. performed the magnetic characterization. All authors wrote and revised the manuscript discussing the results and their presentation.

Data Availability

Data will be made available on request.

Declaration of Competing Interest

The authors declare that they have no known competing financial interests or personal relationships that could have appeared to influence the work reported in this paper.

Acknowledgments

The work has been supported by the Ministerio de Ciencia e Innovación (MCINN) through the projects MAT2015-65445-C2-1-R, MAT2017-86450-C4-1-R, MAT2015-67557-C2-1-P, RTI2018–095856-B-C21, RTI2018–095303-A-C52, PIE: 2021-60-E-030, PIE: 2010-6-OE-013, PID2021-122980OB-C51 and Comunidad de Madrid by S2013/MIT-2850 NANOFRONTMAG and S2018/NMT-4321 NANOMAGCOST. Electron microscopy measurements were carried out at the Centro Nacional de Microscopía Electrónica at the Universidad Complutense de Madrid (ICTS ELECMI, UCM). The authors are grateful to The ESRF (France), MCINN and Consejo Superior de Investigations Científicas (CSIC, Spain) for the provision of synchrotron radiation facilities and to the BM25-SpLine Staff for their support. XAS experiments were also performed at the CLAESS-BL22 beamline at ALBA Synchrotron (Grant no. 2022025654) in collaboration with ALBA staff. Giulio Gorni acknowledges financial support from FJC2020–044866-I /MCIN/AEI/ 10.13039/501100011033 and European Union "NextGenerationEU"/PRTR". A.S. acknowledges financial support from the "Ayudas para contratos Ramón y Cajal" contract No. RYC2021-031236-I.

Appendix A. Supporting information

Supplementary data associated with this article can be found in the online version at doi:10.1016/j.jallcom.2023.170244.

References

[1] R.A. Omar, N. Talreja, D. Chauhan, R. v Mangalaraja, M. Ashfaq, Nano metal-carbon–based materials: emerging platform for the growth and protection of crops, Nanotechnol. -Based Sustain. Altern. Manag. Plant Dis. (2022) 341–354, https://doi.org/10.1016/B978-0-12-823394-8.00013-5

[2] C. Defilippi, M.O.A. Mukadam, S.A. Nicolae, M.R. Lees, C. Giordano, Iron Carbide@ carbon nanocomposites: a tool box of functional materials, Materials 12 (2019) 323, https://doi.org/10.3390/MA12020323

[3] A.A. el Gendy, J.M. Barandiaran, R.L. Hadimani, Magnetic nanostructured materials: from lab to fab, n.d. ⟨http://www.sciencedirect.com:5070/book/9780128139042/magnetic-nanostructured-materials⟩ (Accessed 24 October 2022).

[4] R.C. O'Handley, Modern Magnetic Materials: Principles and Applications, first ed., Wiley-Interscience, 1999.

[5] R.S. Sundar, S.C. Deevi, Soft Magn. FeCo Alloy. Alloy.Dev., Process., Prop. 50 (2013) 157–192, https://doi.org/10.1179/174328005X14339 ⟨Http://Dx.Doi.Org/10.1179/174328005X14339⟩.

[6] A. Shokuhfar, S.S.S. Afghahi, Size controlled synthesis of FeCo alloy nanoparticles and study of the particle size and distribution effects on magnetic properties, Adv. Mater. Sci. Eng. 2014 ()) (2014), https://doi.org/10.1155/2014/295390

[7] K. Zehani, R. Bez, J. Moscovici, F. Mazaleyrat, N. Mliki, L. Bessais, High magnetic moment of FeCo nanoparticles produced in polyol medium, IEEE Trans. Magn. 50 (2014), https://doi.org/10.1109/TMAG.2013.2288411

[8] J. Liu, K. Wu, J.P. Wang, Magnetic properties of cubic FeCo nanoparticles with anisotropic long chain structure, AIP Adv. 6 (2016) 056126, https://doi.org/10.1063/1.4945042

[9] G. Song, M. Kenney, Y.S. Chen, X. Zheng, Y. Deng, Z. Chen, S.X. Wang, S.S. Gambhir, H. Dai, J. Rao, Carbon-coated FeCo nanoparticles as sensitive magnetic-particle-imaging tracers with photothermal and magnetothermal properties, Nat. Biomed. Eng. 2020 4:3 4 (2020) 325–334, https://doi.org/10.1038/s41551-019-0506-0

[10] Ö. Çelik, T. Fırat, Synthesis of FeCo magnetic nanoalloys and investigation of heating properties for magnetic fluid hyperthermia, J. Magn. Magn. Mater. 456 (2018) 11–16, https://doi.org/10.1016/J.JMMM.2018.01.090

[11] S.P. Sherlock, S.M. Tabakman, L. Xie, H. Dai, Photothermally enhanced drug delivery by ultra-small multifunctional feco/graphitic-shell nanocrystals, ACS Nano 5 (2011) 1505, https://doi.org/10.1021/NN103415X

[12] Y. Lei, R. Huang, H. Xie, D. Zhang, X. Liu, Y. Si, N. Li, Electronic structure tuning of FeCo nanoparticles embedded in multi-dimensional carbon matrix for enhanced bifunctional oxygen electrocatalysis, J. Alloy. Compd. 853 (2021) 157070, https://doi.org/10.1016/J.JALLCOM.2020.157070

[13] J. Marbaix, N. Mille, L.M. Lacroix, J.M. Asensio, P.F. Fazzini, K. Soulantica, J. Carrey, B. Chaudret, Tuning the Composition of FeCo Nanoparticle Heating Agents for Magnetically Induced, Catal., ACS Appl. Nano Mater. 3 (2020) 3767–3778, https://doi.org/10.1021/ACSANM.0C00444/ASSET/IMAGES/LARGE/AN0C00444_0012.JPEG

[14] X. Xu, J. Xie, Y. Dai, L. Yang, Z. Cai, B. Jing, J. Zou, FeCo alloys in-situ formed in Co/Co2P/N-doped carbon as a durable catalyst for boosting bio-electrons-driven oxygen reduction in microbial fuel cells, Int J. Hydrog. Energy 47 (2022) 3063–3074, https://doi.org/10.1016/J.IJHYDENE.2021.10.199

[15] J.H. Park, S. Woo, J. Lee, H.Y. Jung, J.C. Ro, C. Park, B. Lim, S.J. Suh, Facile modified polyol synthesis of FeCo nanoparticles with oxyhydroxide surface layer as efficient oxygen evolution reaction electrocatalysts, Int J. Hydrog. Energy 46 (2021) 15398–15409, https://doi.org/10.1016/J.IJHYDENE.2021.02.027

[16] W. Chu, Y. Wang, Y. Du, R. Qiang, C. Tian, X. Han, FeCo alloy nanoparticles supported on ordered mesoporous carbon for enhanced microwave absorption, J. Mater. Sci. 52 (2017) 13636–13649, https://doi.org/10.1007/S10853-017-1439-1/FIGURES/10

[17] J. Chen, J. Zheng, Q. Huang, F. Wang, G. Ji, Enhanced microwave absorbing ability of carbon fibers with embedded FeCo/CoFe2O4nanoparticles, ACS Appl. Mater. Interfaces 13 (2021) 36182–36189, https://doi.org/10.1021/ACSAMI.1C09430/ASSET/IMAGES/LARGE/AM1C09430_0008.JPEG

[18] V. Vadillo, A. Gómez, J. Berasategi, J. Gutiérrez, M. Insausti, I. Gil de Muro, J.S. Garitaonandia, A. Arbe, A. Iturrospe, M.M. Bou-Ali, J.M. Barandiarán, High magnetization FeCo nanoparticles for magnetorheological fluids with enhanced response, Soft Matter 17 (2021) 840–852, https://doi.org/10.1039/D0SM01702G

[19] M. v Puydinger Dos Santos, S. Barth, F. Béron, K.R. Pirota, A.L. Pinto, J.P. Sinnecker, S. Moshkalev, J.A. Diniz, I. Utke, Magnetoelectrical transport improvements of postgrowth annealed iron-cobalt nanocomposites: a possible route for future room-temperature spintronics, ACS Appl. Nano Mater. 1 (2018) 3364–3374, https://doi.org/10.1021/ACSANM.8B00581/ASSET/IMAGES/LARGE/AN-2018-00581X_0006.JPEG

[20] G. Song, M. Kenney, Y.S. Chen, X. Zheng, Y. Deng, Z. Chen, S.X. Wang, S.S. Gambhir, H. Dai, J. Rao, Carbon-coated FeCo nanoparticles as sensitive magnetic-particle-imaging tracers with photothermal and magnetothermal properties, Nat. Biomed. Eng. 2020 4:3 4 (2020) 325–334, https://doi.org/10.1038/s41551-019-0506-0

[21] N. Patelli, F. Cugini, D. Wang, S. Sanna, M. Solzi, H. Hahn, L. Pasquini, Structure and magnetic properties of Fe-Co alloy nanoparticles synthesized by pulsed-laser inert gas condensation, J. Alloy. Compd. 890 (2022) 161863, https://doi.org/10.1016/J.JALLCOM.2021.161863

[22] G. Khadra, A. Tamion, F. Tournus, O. Boisron, C. Albin, V. Dupuis, Structure and magnetic properties of FECO clusters: carbon environment and annealing effects, J. Phys. Chem. C. 121 (2017) 10713–10718, https://doi.org/10.1021/ACS.JPCC.6B10715/ASSET/IMAGES/JP-2016-10715S_M001.GIF

[23] J. Bai, Y.H. Xu, J.P. Wang, Cubic and spherical high-moment FeCo nanoparticles with narrow size distribution, IEEE Trans. Magn. 43 (2007) 3340–3342, https://doi.org/10.1109/TMAG.2007.893781

[24] F. Sánchez-De Jesús, A.M. Bolarín-Miró, C.A. Cortés Escobedo, G. Torres-Villaseñor, P. Vera-Serna, Structural analysis and magnetic properties of FeCo alloys obtained by mechanical alloying, J. Metall. 2016 (2016) 1–8, https://doi.org/10.1155/2016/8347063

[25] P. Nautiyal, M.M. Seikh, O.I. Lebedev, A.K. Kundu, Sol–gel synthesis of Fe–Co nanoparticles and magnetization study, J. Magn. Magn. Mater. 377 (2015) 402–405, https://doi.org/10.1016/J.JMMM.2014.10.157

[26] R. Kuchi, K.M. Lee, Y. Lee, C.H. Luong, K.D. Lee, B.G. Park, J.R. Jeong, Synthesis of highly magnetic feco nanoparticles through a one pot polyol process using all metal chlorides precursors with precise composition tunability, Nanosci. Nanotechnol. Lett. 7 (2015) 734–737, https://doi.org/10.1166/NNL.2015.2016

[27] D.M. Clifford, C.E. Castano, A.J. Lu, E.E. Carpenter, Synthesis of FeCo alloy magnetically aligned linear chains by the polyol process: structural and magnetic characterization, J. Mater. Chem. C. Mater. 3 (2015) 11029–11035, https://doi.org/10.1039/C5TC02058A

[28] P. Karipoth, A. Thirumurugan, S. Velaga, J.M. Greneche, R. Justin Joseyphus, Magnetic properties of FeCo alloy nanoparticles synthesized through instant chemical reduction, J. Appl. Phys. 120 (2016) 123906, https://doi.org/10.1063/1.4962637

[29] L.F. Julio Jimenez, A. Herrera Barros, Z.I. Caamaño De Ávila, Synthesis and characterization of Fe55Co45 magnetic nanoparticles by polyol and green chemistry method, Results Phys. 15 (2019) 102785, https://doi.org/10.1016/J.RINP.2019.102785

[30] J.-H. Park, S.-H. Shin, S.-H. Kim, J.-K. Park, J.-W. Lee, J.-H. Shin, J.-H. Park, S.-W. Kim, H.-J. Choi, K.-S. Lee, J.-C. Ro, C. Park, S.-J. Suh, Effect of synthesis time and composition on magnetic properties of FeCo nanoparticles by polyol method, J. Nanosci. Nanotechnol. 18 (2018) 7115–7119, https://doi.org/10.1166/JNN.2018.15477

[31] J.H. Park, C. Park, K.S. Lee, S.J. Suh, Effect of NaOH and precursor concentration on size and magnetic properties of FeCo nanoparticles synthesized using the polyol method, AIP Adv. 10 (2020) 115220, https://doi.org/10.1063/5.0024622

[32] S. Moditma, G. Choudhary, V.R. Vashisht, S. Reddy, Annapoorni, facile synthesis of highly magnetic long-term stable FeCo Nanoparticles, J. Supercond. Nov. Magn. 33 (2020) 1653–1657, https://doi.org/10.1007/S10948-019-05398-W/TABLES/1

[33] D.F. Dias, T.P. Braga, J.M. Soares, J.M. Sasaki, Structural, morphological and magnetic properties of FeCo-$(Fe,Co)_3O_4$ nanocomposite synthesized by proteic sol-gel method using a rotary oven, Mater. Res. 22 (2019), https://doi.org/10.1590/1980-5373-MR-2018-0446

[34] P. Nautiyal, M.M. Seikh, O.I. Lebedev, A.K. Kundu, Sol–gel synthesis of Fe–Co nanoparticles and magnetization study, J. Magn. Magn. Mater. 377 (2015) 402–405, https://doi.org/10.1016/J.JMMM.2014.10.157

[35] G.S. Chaubey, C. Barcena, N. Poudyal, C. Rong, J. Gao, S. Sun, J.P. Liu, Synthesis and stabilization of FeCo nanoparticles, J. Am. Chem. Soc. 129 (2007) 7214–7215, https://doi.org/10.1021/ja0708969

[36] S. Koutsopoulos, R. Barfod, K.M. Eriksen, R. Fehrmann, Synthesis and characterization of iron-cobalt (FeCo) alloy nanoparticles supported on carbon, J. Alloy. Compd. 725 (2017) 1210–1216, https://doi.org/10.1016/J.JALLCOM.2017.07.105

[37] S.Q. Wu, B. Balamurugan, X. Zhao, S. Yu, M.C. Nguyen, Y. Sun, S.R. Valloppilly, D.J. Sellmyer, K.M. Ho, C.Z. Wang, Exploring new phases of Fe3−xCoxC for rare-earth-free magnets, J. Phys. D. Appl. Phys. 50 (2017) 215005, https://doi.org/10.1088/1361-6463/AA6B85

[38] V.I. Razumovskiy, G. Ghosh, A first-principles study of cementite (Fe3C) and its alloyed counterparts: structural properties, stability, and electronic structure, Comput. Mater. Sci. 110 (2015) 169–181, https://doi.org/10.1016/J.COMMATSCI.2015.08.006

[39] H.K.D.H. Bhadeshia, Cementite 65 (2019) 1–27, https://doi.org/10.1080/09506608.2018.1560984 ⟨Https://Doi.Org/10.1080/09506608.2018.1560984⟩.

[40] A. Gangwar, G. Singh, S.K. Shaw, R.K. Mandal, A. Sharma, S.S. Meena, C.L. Prajapat, N.K. Prasad, Synthesis and structural characterization of CoxFe3−xC ($0 \le x \le 0.3$) magnetic nanoparticles for biomedical applications, N. J. Chem. 43 (2019) 3536–3544, https://doi.org/10.1039/C8NJ05240A

[41] A.A. El-Gendy, M. Bertino, D. Clifford, M. Qian, S.N. Khanna, E.E. Carpenter, Experimental evidence for the formation of CoFe2C phase with colossal magnetocrystalline-anisotropy, Appl. Phys. Lett. 106 (2015) 213109, https://doi.org/10.1063/1.4921789

[42] E.K. Delczeg-Czirjak, A. Edström, M. Werwiński, J. Rusz, N. v. Skorodumova, L. Vitos, O. Eriksson, Stabilization of the tetragonal distortion of Fe x Co 1-x alloys by C impurities: a potential new permanent magnet, Phys. Rev. B Condens Matter Mater. Phys. 89 (2014) 144403, https://doi.org/10.1103/PHYSREVB.89.144403/FIGURES/4/MEDIUM

[43] T. Burkert, L. Nordström, O. Eriksson, O. Heinonen, Giant magnetic anisotropy in tetragonal FeCo alloys, Phys. Rev. Lett. 93 (2004) 027203, https://doi.org/10.1103/PHYSREVLETT.93.027203/FIGURES/3/MEDIUM

[44] T. Hasegawa, T. Niibori, Y. Takemasa, M. Oikawa, Stabilisation of tetragonal FeCo structure with high magnetic anisotropy by the addition of V and N elements, Sci. Rep. 2019 9:1 9 (2019) 1–9, https://doi.org/10.1038/s41598-019-41825-7

[45] M. Gong, A. Kirkeminde, M. Wuttig, S. Ren, Phase transformation-induced tetragonal FeCo nanostructures, Nano Lett. 14 (2014) 6493–6498, https://doi.org/10.1021/NL5030485/SUPPL_FILE/NL5030485_SI_001.PDF

[46] S.S. Tan, N. Wang, C.Q. Yang, L. Wang, Y. Hu, J. Li, S.C. Xu, M. Lu, H.B. Li, Exchange bias and exchange spring in CoFe2O4/FeO/CoFe nanocomposites, J. Magn. Magn. Mater. 556 (2022), https://doi.org/10.1016/J.JMMM.2022.169428

[47] G.C.P. Leite, E.F. Chagas, R. Pereira, R.J. Prado, A.J. Terezo, M. Alzamora, E. Baggio-Saitovitch, Exchange coupling behavior in bimagnetic CoFe2O4/CoFe2 nanocomposite, J. Magn. Magn. Mater. 324 (2012) 2711–2716, https://doi.org/10.1016/J.JMMM.2012.03.034

[48] S.S. Tan, N. Wang, C.Q. Yang, L. Wang, Y. Hu, J. Li, S.C. Xu, M. Lu, H.B. Li, Exchange bias and exchange spring in CoFe2O4/FeO/CoFe nanocomposites, J. Magn. Magn. Mater. 556 (2022), https://doi.org/10.1016/J.JMMM.2022.169428

[49] S.M. Liuzzo, N. Carmignani, J. Chavanne, V. Cerantola, A. Dorothea Rosa, Z. Konôpková, al -, C. Ponchut, J. Rigal, J. Cíement, E. Papillon, A. Homs, S. Petitdemange, MAXIPIX, a fast readout photon-counting X-ray area detector for synchrotron applications, J. Instrum. 6 (2011) C01069, https://doi.org/10.1088/1748-0221/6/01/C01069

[50] S. Roobol, W. Onderwaater, J. Drnec, R. Felici, J. Frenken, BINoculars: data reduction and analysis software for two-dimensional detectors in surface X-ray diffraction, Urn:Issn:1600-5767 48 (2015) 1324–1329, https://doi.org/10.1107/S1600576715009607

[51] N. Doebelin, R. Kleeberg, Profex: a graphical user interface for the Rietveld refinement program BGMN, J. Appl. Crystallogr 48 (2015) 1573–1580, https://doi.org/10.1107/S1600576715014685

[52] M. Bosman, M. Watanabe, D.T.L. Alexander, V.J. Keast, Mapping chemical and bonding information using multivariate analysis of electron energy-loss spectrum images, Ultramicroscopy 106 (2006) 1024–1032, https://doi.org/10.1016/j.ultramic.2006.04.016

[53] ImageJ, (n.d.). ⟨https://imagej.nih.gov/ij/index.html⟩ (Accessed 7 December 2022).
[54] L. Simonelli, C. Marini, W. Olszewski, M. Ávila Pérez, N. Ramanan, G. Guilera, V. Cuartero, K. Klementiev, CLÆSS: hard X-ray Absorpt. beamline ALBA CELLS Synchrotron 3 (2016), https://doi.org/10.1080/23311940.2016.1231987 ⟨Http://Www.Editorialmanager.Com/Cogentphys⟩.
[55] M. Newville, B. Ravel, D. Haskel, E.A. Stern, Y. Yacoby, Analysis of Multiple Scattering XAFS Data using Theoretical Standards, (1995).
[56] A. Castellano-Soria, J. López-Sánchez, C. Granados-Miralles, M. Varela, E. Navarro, C. González, P. Marín, Novel one-pot sol-gel synthesis route of Fe3C/few-layered graphene core/shell nanoparticles embedded in a carbon matrix, J. Alloy. Compd. 902 (2022) 163662, https://doi.org/10.1016/J.JALLCOM.2022.163662
[57] G.S. Grebenyuk, Y. Lobanova, D.A. Smirnov, A.N. Popova, Synthesis and characterization of iron-cobalt nanoparticles, J. Phys. Conf. Ser. 345 (2012) 012030, https://doi.org/10.1088/1742-6596/345/1/012030
[58] C. Z, Q. M, Z. C, G. Y, J. B, Facile route for synthesis of mesoporous graphite encapsulated iron carbide/iron nanosheet composites and their electrocatalytic activity, J. Colloid Interface Sci. 491 (2017) 55–63, https://doi.org/10.1016/J.JCIS.2016.11.086
[59] D. Hardeman, S. Esconjauregui, R. Cartwright, S. Bhardwaj, L. D'Arsié, D. Oakes, J. Clark, C. Cepek, C. Ducati, J. Robertson, The synergistic effect in the Fe-Co bimetallic catalyst system for the growth of carbon nanotube forests, J. Appl. Phys. 117 (2015) 044308, https://doi.org/10.1063/1.4906846
[60] M.P. Dojcinovic, Z.Z. Vasiljevic, V.P. Pavlovic, D. Barisic, D. Pajic, N.B. Tadic, M.V. Nikolic, Mixed Mg–Co spinel ferrites: structure, morphology, magnetic and photocatalytic properties, J. Alloy. Compd. 855 (2021), https://doi.org/10.1016/J.JALLCOM.2020.157429
[61] T.A.S. Ferreira, J.C. Waerenborgh, M.R. Nunes, M.H.R.M. Mendonca, F.M. Costa, Structural and morphological characterization of Fe Co2 O4 and Co Fe2 O4 spinels prepared by a coprecipitation method, 2003.
[62] E.R. Jette, F. Foote, An x-ray study of the wuestite (Fe O) solid solutions, 1933.
[63] S. Sasaki, K. Fujino, Y. Takéuchi, X-Ray Determination of Electron-Density Distributions in Oxides, MgO, MnO, CoO, and NiO, and Atomic Scattering Factors of their Constituent Atoms, 1979 .
[64] A. Khort, S. Roslyakov, P.L.-N.-S.& Nano-Objects, undefined 2021, Solution combustion synthesis of single-phase bimetallic nanomaterials, Elsevier. (n.d.). ⟨https://www.sciencedirect.com/science/article/pii/S2352507X21000329⟩ (Accessed 6 September 2022).
[65] N.C. Shin, Y.H. Lee, Y.H. Shin, J. Kim, Y.W. Lee, Synthesis of cobalt nanoparticles in supercritical methanol, Mater. Chem. Phys. 124 (2010) 140–144, https://doi.org/10.1016/J.MATCHEMPHYS.2010.06.005
[66] P.E.A.O.M.A. D.Sc., E.L.Y. M.Sc., XLI, Https://Doi.Org/10.1080/14786443309462199, recision Meas. Cryst. Parameters 15 (2009) 472–488, https://doi.org/10.1080/14786443309462199
[67] H. Chen, Y. Yu, H.L. Xin, K.A. Newton, M.E. Holtz, D. Wang, D.A. Muller, Héctor, H.D. Abruñ, F.J. Disalvo, Synthetic and mechanistic advances in nanocrystal growth dx, Chem. Mater. 25 (2013) 1436–1442, https://doi.org/10.1021/cm303489z
[68] S. Mourdikoudis, K. Simeonidis, M. Angelakeris, I. Tsiaoussis, O. Kalogirou, C. Desvaux, C. Amiens, B. Chaudret, Eff. AIR EXPOSURE Struct. Magn. FEATURES FeCo NANOPARTICLES 21 (2011) 1161–1168, https://doi.org/10.1142/S0217984907013869 ⟨Http://Dx.Doi.Org/10.1142/S0217984907013869⟩.
[69] A.A. Guda, S.A. Guda, A. Martini, A.N. Kravtsova, A. Algasov, A. Bugaev, S.P. Kubrin, L. v Guda, P. Šot, J.A. van Bokhoven, C. Copéret, A. v Soldatov, Understanding X-ray absorption spectra by means of descriptors and machine learning algorithms, Npj Comput. Mater. 2021 7:1 7 (2021) 1–13, https://doi.org/10.1038/s41524-021-00664-9
[70] J. Rubio-Zuazo, A. Chainani, M. Taguchi, D. Malterre, A. Serrano, G.R. Castro, Electronic structure of FeO, γ-Fe2 O3, and Fe3 O4 epitaxial films using high-energy spectroscopies, Phys. Rev. B. 97 (2018) 235148, https://doi.org/10.1103/PHYSREVB.97.235148/FIGURES/10/MEDIUM
[71] M. Abuín, A. Serrano, J. Chaboy, M.A. García, N. Carmona, XAS study of Mn, Fe and Cu as indicators of historical glass decay, J. Anal. Spectrom. 28 (2013) 1118–1124, https://doi.org/10.1039/C3JA30374H
[72] D. Malferrari, E. Castellini, F. Bernini, A.S. Rubio, G.R. Castro, C.I. Sainz-Díaz, M. Caleffi, M.F. Brigatti, M. Borsari, Chemical trapping of gaseous H2S at high and low partial pressures by an iron complex immobilized inside the montmorillonite interlayer, Microporous Mesoporous Mater. 265 (2018) 8–17, https://doi.org/10.1016/J.MICROMESO.2018.01.017
[73] J.B..Kortrijht. K. Kim, X-Ray Data Booklet Authors, 1986. (n.d.). ⟨https://www.yumpu.com/en/document/view/28975275/x-ray-data-booklet-authors⟩ (accessed September 19, 2022).
[74] Z.Y. Liu, J.L. Zhu, X. Tong, S. Niu, W.Y. Zhao, A review of CoSb3-based skutterudite thermoelectric materials, J. Adv. Ceram. 9 (2020) 647–673, https://doi.org/10.1007/S40145-020-0407-4
[75] B. Westerstrand, P. Nordblad, L. Nordborg, The magnetocrystalline anisotropy constants of iron and iron-silicon alloys, Phys. Scr. 11 (1975) 383, https://doi.org/10.1088/0031-8949/11/6/010
[76] S. Yamamoto, T. Terai, T. Fukuda, K. Sato, T. Kakeshita, S. Horii, M. Ito, M. Yonemura, Magnetocrystalline anisotropy of cementite pseudo single crystal fabricated under a rotating magnetic field, J. Magn. Magn. Mater. 451 (2018) 1–4, https://doi.org/10.1016/J.JMMM.2017.10.114
[77] J. Crangle, G.M. Goodman, The Magnetization of Pure Iron and Nickel, 1971. https://doi.org/10.1098/rspa.1971.0044.
[78] G. Fan, Y. Jiang, J. Xin, Z. Zhang, X. Fu, P. Xie, C. Cheng, Y. Liu, Y. Qu, K. Sun, R. Fan, Facile Synthesis of Fe@Fe3C/C nanocomposites derived from bulrush for excellent electromagnetic wave-absorbing properties, ACS Sustain. Chem. Eng. 7 (2019) 18765–18774, https://doi.org/10.1021/ACSSUSCHEMENG.9B02913/ASSET/IMAGES/LARGE/SC9B02913_0008.JPEG
[79] P. Zhang, X. Wang, W. Wang, X. Lei, H. Yang, Iron carbide and nitride via a flexible route: synthesis, structure and magnetic properties, RSC Adv. 5 (2015) 21670–21674, https://doi.org/10.1039/C5RA00336A
[80] Y.T. Chen, S.U. Jen, Y.D. Yao, J.M. Wu, C.C. Lee, A.C. Sun, Magnetic properties of face-centered cubic co films, IEEE Trans. Magn. 42 (2006) 278–282, https://doi.org/10.1109/TMAG.2005.861468
[81] B. Balasubramanian, P. Mukherjee, R. Skomski, P. Manchanda, B. Das, D.J. Sellmyer, Magnetic nanostructuring and overcoming Brown's paradox to realize extraordinary high-temperature energy products, Sci. Rep. 2014 4:1 4 (2014) 1–6, https://doi.org/10.1038/srep06265
[82] G. Herzer, Nanocrystalline soft magnetic materials, J. Magn. Magn. Mater. 112 (1992) 258–262, https://doi.org/10.1016/0304-8853(92)91168-S
[83] A. Wu, X. Yang, H. Yang, Magnetic properties of carbon-encapsulated Fe–Co alloy nanoparticles, Dalton Trans. 42 (2013) 4978–4984, https://doi.org/10.1039/C3DT32639J
[84] M. Woińska, J. Szczytko, A. Majhofer, J. Gosk, K. Dziatkowski, A. Twardowski, Magnetic interactions in an ensemble of cubic nanoparticles: a Monte Carlo study, Phys. Rev. B Condens Matter Mater. Phys. 88 (2013), https://doi.org/10.1103/PHYSREVB.88.144421
[85] E.H. Sánchez, M. Vasilakaki, S.S. Lee, P.S. Normile, M.S. Andersson, R. Mathieu, A. López-Ortega, B.P. Pichon, D. Peddis, C. Binns, P. Nordblad, K. Trohidou, J. Nogués, J.A. de Toro, Crossover from individual to collective magnetism in dense nanoparticle systems: local anisotropy versus dipolar interactions, Small 18 (2022) 2106762, https://doi.org/10.1002/SMLL.202106762
[86] E.L. Verde, G.T. Landi, M.S. Carrião, A.L. Drummond, J.A. Gomes, E.D. Vieira, M.H. Sousa, A.F. Bakuzis, Field dependent transition to the non-linear regime in magnetic hyperthermia experiments: comparison between maghemite, copper, zinc, nickel and cobalt ferrite nanoparticles of similar sizes, AIP Adv. 2 (2012) 032120, https://doi.org/10.1063/1.4739533
[87] F. Wang, X. Xue, G. Wang, J. Cai, X. Fu, Prep. Charact. FeCo Alloy Nanopart. 128 (2011) 177–182, https://doi.org/10.1080/10584587.2011.576634 ⟨Http://Dx.Doi.Org/10.1080/10584587.2011.576634⟩.
[88] S. Moditma, G. Choudhary, V.R. Vashisht, S. Reddy, Annapoorni, facile synthesis of highly magnetic long-term stable FeCo Nanoparticles, J. Supercond. Nov. Magn. 33 (2020) 1653–1657, https://doi.org/10.1007/S10948-019-05398-W/TABLES/1